Available online at www.sciencedirect.com
SCIENCE DIRECT
Journal of Power Sources 157 (2006) 368–376
JOURNAL OF POWER SOURCES
www.elsevier.com/locate/jpowsour

Heat resistant alloys as interconnect materials of reduced temperature SOFCs

Li Jian [a,*], Pu Jian [a], Xie Guangyuan [b], Wang Shunxu [a], Xiao Jianzhong [a]

[a] *School of Materials Science and Engineering, State Key Laboratory of Plastic Forming Simulation and Die and Mould Technology, Huazhong University of Science and Technology, Wuhan, Hubei 430074, PR China*

[b] *School of Materials Science and Metallurgical Engineering, Wuhan University of Science and Technology, Wuhan, Hubei 430080, PR China*

Received 17 June 2005; accepted 27 July 2005
Available online 19 October 2005

Abstract

Heat-resistant alloys, Haynes 230 and SS310, were exposed to air and humidified H_2 at 750 °C for up to 1000 h, respectively, simulating the environments in reduced temperature solid oxide fuel cells (SOFCs). The oxidized samples were characterized by using SEM, EDS and X-ray diffraction to obtain the morphology, thickness, composition and crystal structure of the oxide scales. A mechanism for the formation of metallic Ni-rich nodules on top of the oxide scale in Haynes 230 sample oxidized in humidified H_2 was established. Thermodynamic analysis confirmed that $MnCr_2O_4$ is the favored spinel phase, together with Cr_2O_3, in the oxide scales.

Keywords: Heat-resistant alloys; Metallic interconnects; Oxidation; Solid oxide fuel cells

1. Introduction

Among the most critical needs for the commercial deployment of SOFCs are the interconnects, which separate the fuel and oxidant gases and provide electric connection between the anode and cathode of adjacent cells that permits an in-series voltage connection of individual fuel cell elements. In some stack constructions, the interconnect also is a structural element employed to maintain the mechanical stability of the stack and to offer mechanical connection surfaces for gas path sealing. Therefore, close thermal expansion match to the fuel cell components, sufficient electronic conduction at the operation temperature, good chemical stability and compatibility in both reducing and oxidizing environments and adequate thermal cyclicability are fundamental requirements for the interconnect materials.

Complex perovskite ceramic oxides, typically the Sr- or Ca-doped $LaCrO_3$, have been selected as interconnect materials for high temperature SOFCs operated at ~1000 °C [1–3]. No other ceramic materials have been identified to replace the doped $LaCrO_3$. However, ceramic interconnects are mechanically brittle, difficult to manufacture in various forms, deforms due to the loss of oxygen at the fuel-side, and represents significant portion of the product cost in SOFC stacks. With lowering operation temperatures, further study in ceramic interconnect materials appears unlikely.

Cr-based alloy Cr–5Fe–1Y_2O_3 is a well-known metallic material proposed for planar high-temperature SOFC interconnect. It is a pre-alloyed oxide dispersion strengthened (ODS) material; therefore, material cost is significant. The sintered Cr–5Fe–1Y_2O_3 offers thermal expansion compatibility with stabilized zirconia and excellent oxidation resistance [4], however, rapid electrochemical degradation was observed with the interconnect. This degradation was found to be related to the evaporation of volatile Cr species from the interconnect followed by its deposition on the cathode surface [5], spinels and perovskites [5,6] were suggested as coatings to prevent the damage.

A major benefit of lower temperature SOFC operation (650–750 °C) is the anticipation that interconnect materials with lower cost, better formability and toughness, and simpler fabrication processing steps can be employed to replace the oxide based materials required at higher temperatures. Metallic materials have drawn more and more attention as interconnect materials in the development of the reduced temperature SOFCs

* Corresponding author. Tel.: +86 27 87557694; fax: +86 27 87544307.
E-mail address: plumarrow@126.com (L. Jian).

0378-7753/$ – see front matter © 2005 Elsevier B.V. All rights reserved.
doi:10.1016/j.jpowsour.2005.07.086

[2,3,7,8], offering excellent ductility, higher electronic conductivity, higher heat conductivity, lower cost and flexible fabricability. Significant performance enhancement and cost advantage can be realized. However, metallic interconnects have not been successfully deployed since the oxidation of metallic materials forms an electrically insulating surface oxide, leading to undesirable increase in contact electrical resistance. The mismatch in thermal expansion coefficient between the metallic materials and cell component materials (electrolyte and electrodes) has been recognized to cause the interfacial contact breakdown.

Oxidation-resistant alloys are generally considered to be the candidate materials for reduced temperature SOFC interconnects. Such alloys contain Cr and/or Al as the alloying elements to form a protective oxide scale, by preferential oxidation of Cr (Cr_2O_3) or Al (Al_2O_3). Al_2O_3-forming alloys are less interesting for SOFC interconnect applications due to the low electrical conductivity of the oxide scale. Recent studies have focused on the Cr_2O_3-forming alloys, especially the Cr-containing ferritic stainless steels [9–19] with a thermal expansion coefficient in the neighborhood of 12×10^{-6}. This type of alloys forms mainly Cr_2O_3 as the protecting scale and Cr–Mn spinel. Austenitic alloys, such as austenitic stainless steels and superalloys [20–22] have rarely been evaluated as interconnect candidate materials due to their relatively high thermal expansion coefficients.

The objective of the present study was to evaluate a Ni-based alloy Haynes 230 and an austenitic stainless steel SS310 for the application to the interconnect component of the reduced temperature SOFCs. Oxidation behavior in both cathodic oxidizing and anodic reducing environments, specifically the surface morphology, thickness, crystal structure and composition of the oxide scales. Haynes 230 and SS310 have mean coefficients of thermal expansion (CTE) 15.2×10^{-6} [23] and 18×10^{-6} between 25 and 800 °C, respectively, which are slightly higher than that of the SOFC cell components ($10–13 \times 10^{-6}$ [24]), however, it is believed that the difficulty caused by the minor mismatch in CTEs can be alleviated through the design of the SOFC interconnect and stack configuration.

2. Experimental

2.1. Materials

Commercial Haynes 230 alloy and SS310 sheet metals (∼1 mm thick) were provided by Haynes International and Liyuan Precision Materials, respectively. The nominal composition of the alloys is listed in Table 1.

Coupon samples with dimensions of 25 mm × 25 mm were cut by an electron discharge machine. All surfaces of the samples were mechanically polished with 1200-grit sand papers and ultrasonically cleaned before the oxidation tests.

2.2. Oxidation

The samples were oxidized in both oxidizing and reducing environments at 750 °C for up to 1000 h, respectively, simulating the operation conditions of the reduced temperature SOFCs. The oxidizing atmosphere was air and the reducing atmosphere was humidified H_2 through a water bubbler at 65 °C.

2.3. Characterization

The oxidized samples were characterized by using a FEI Sirion 200 field emission scanning electron microscope (SEM) with energy dissipation spectrum (EDS) attachment, in terms of surface oxide morphology, oxide thickness and composition. The samples for the cross-section examination were mounted in Buhler epoxide and polished by using a Buhler automatic polisher. A PANalytical X'Pert PRO X-ray diffractometer was used to identify the phases in the oxide scales under the conditions of 40 mA and 40 kV; the scanning rate was 10 degree min^{-1}, and the 2θ angle ranged from 20° to 80°.

3. Results

3.1. Morphology of surface oxides

The morphologies of the surface oxide scales of Haynes 230 alloy and SS310 stainless steel are dramatically different. Figs. 1 and 2 are the surface oxide SEM micrographs of Haynes 230 and SS310 samples at lower magnification (×1000) oxidized in air at 750 °C for 1000 h. In both samples, all the grain

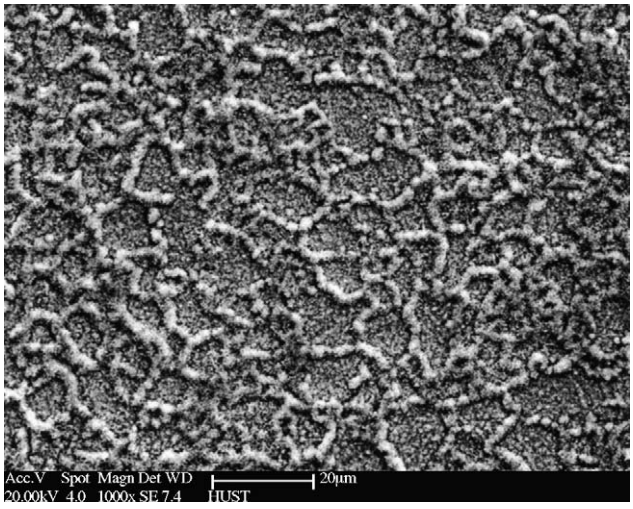

Fig. 1. SEM micrograph of the surface oxide morphology of Haynes 230 exposed to air at 750 °C for 1000 h, the grain boundaries are outlined by the oxide bulges.

Table 1
Chemical composition (wt%) of Haynes 230 and SS310 stainless steel

	Ni	Cr	W	Mo	Mn	Si	Al	C	La	Co	Fe	B
Haynes 230	57	22	14	2.0	0.5	0.4	0.3	0.1	0.02	5.0	3.0	0.01
SS310	19–22	24–26	–	–	<2.0	<1.0	–	<0.1	–	–	Bal	–

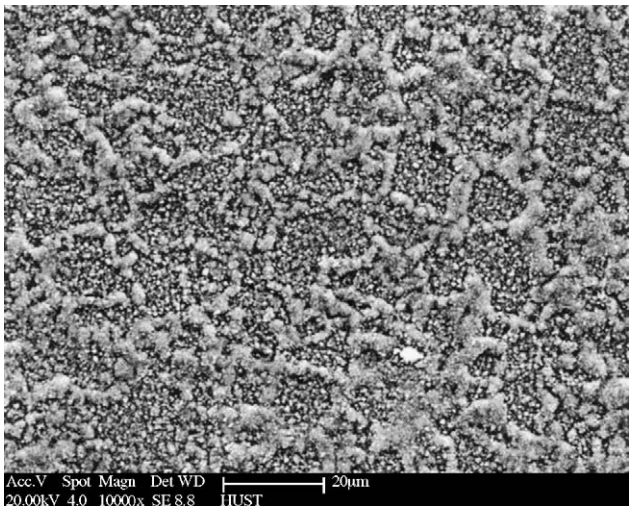

Fig. 2. SEM micrograph of the surface oxide morphology of SS310 exposed to air at 750 °C for 1000 h, the grain boundaries are outlined by the oxide relieves.

boundaries are outlined by the grain-boundary oxide network that is higher than the grain surfaces; and inside the grains, the scale is consisting of granular oxides. At a higher magnification (×10,000), it can be clearly noticed that the grain-boundary oxide network on the oxidized Haynes 230 alloy surface contains whisker (or needle-like) and granular oxides, as shown in Fig. 3, and in the situation of SS310 stainless steel, Fig. 4, the needle-like oxides are disappeared, only well-crystallized oxide particles can be observed that are much coarser in dimension compared to that in the Haynes 230 sample. At grain boundaries, the diffusion of metal ions was facilitated since the diffusion coefficient of grain-boundary is orders of magnitude higher than that of the grains, resulting in the oxide bulges along the grain boundaries. Inside the grains, the microstructure of oxide scale of Haynes 230 alloy is finer and denser than that of SS310 stainless steel.

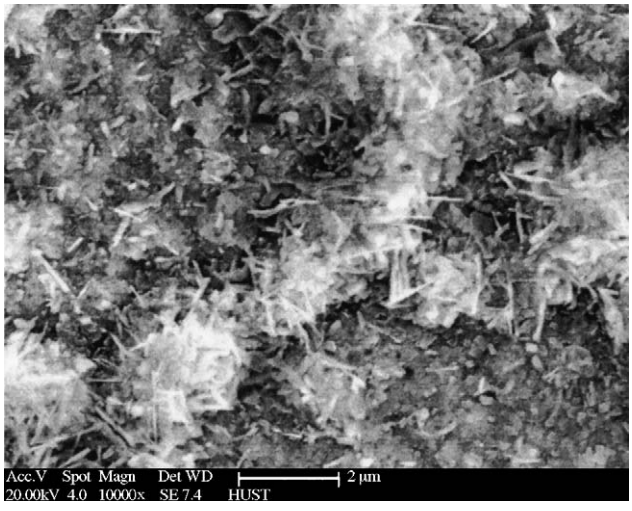

Fig. 3. Higher magnification SEM micrograph of the surface oxide morphology of Haynes 230 oxidized in air at 750 °C for 1000 h, showing oxide whiskers along the grain boundaries and uniform fine oxides within the grains.

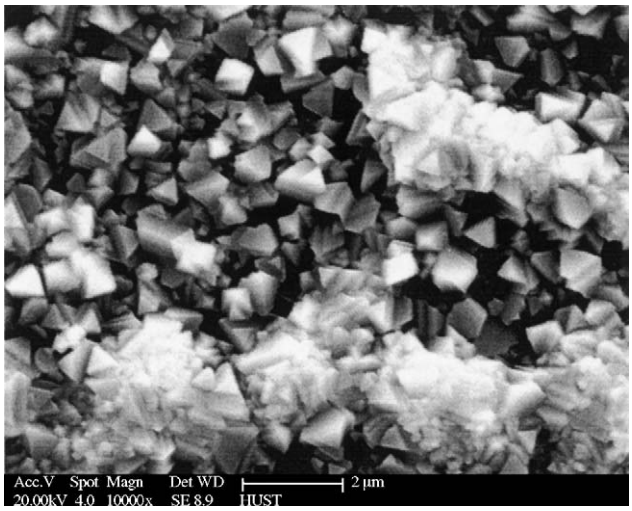

Fig. 4. Higher magnification SEM micrograph of the surface oxide morphology of SS310 oxidized in air at 750 °C for 1000 h, showing densely packed and well crystallized oxides along the grain boundaries and loosely arranged oxide particles within the grains.

Figs. 5 and 6 show the lower magnification (×1000) SEM morphologies of Haynes 230 alloy and SS310 stainless steel oxidized in humidified H_2 atmosphere at 750 °C for 1000 h, respectively. For the Haynes 230 sample, the oxidized surface is featured by shining metallic nodules distributed within the grains on the background of fine and dense oxide microstructure, and the strip areas with much less such nodules depict the grain boundaries, which is not seen in the sample oxidized in air. The nodules nucleated individually, and coalescence of nodules happened as a consequence of continuous growth of the originally separated nodules. This observation was briefly reported previously [22], and will be discussed in more detail in subsequent sections. For the SS310 sample, the oxide particles inside the grain are triangularly shaped with a specific facet parallel to the surface, and the oxide particles along the grain boundaries are more or less rounded, as obviously seen in Fig. 7.

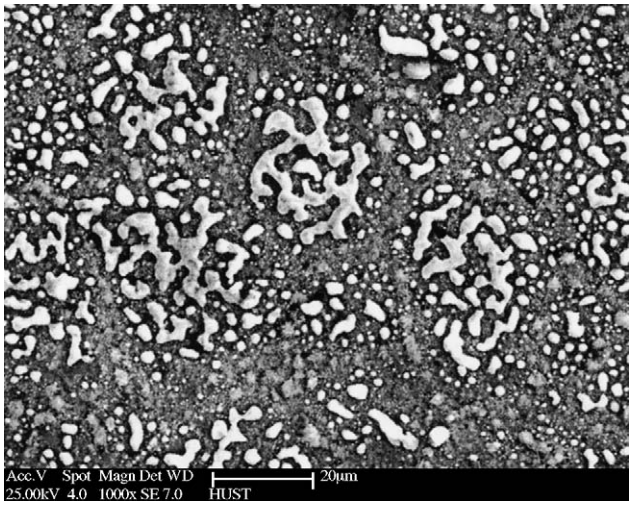

Fig. 5. SEM micrograph of the surface morphology of Haynes 230 after exposure to humidified H_2 at 750 °C for 1000 h, shining metallic nodules formed inside the grains and much less along the grain boundaries.

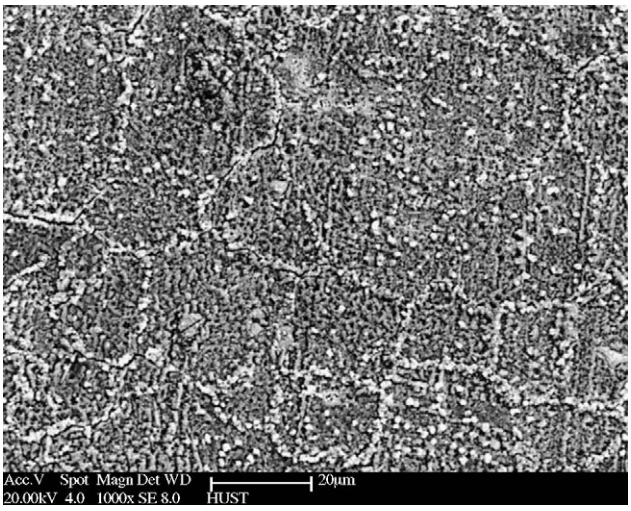

Fig. 6. SEM micrograph of the surface morphology of SS310 after exposure to humidified H_2 at 750 °C for 1000 h.

3.2. Scale thickness and composition

Figs. 8–11 show the SEM micrographs of the cross-sections of Haynes 230 alloy and SS310 stainless steel oxidized in air and humidified H_2 at 750 °C for 1000 h, respectively. The thickness of the oxide formed in each situation is around 1 μm thick. For Haynes 230 oxidized in both atmospheres, the oxide scale adheres to the alloy substrate tightly; no voids and cracks are observed, suggesting a high resistance to the oxide scale spallation. The shining metallic nodules shown in the sample of Haynes 230 oxidized in humidified H_2, Fig. 9, locate on top of the oxide scale, thinner oxide scale corresponds to a smaller nodule size. However, in the cases of SS310 stainless steel, cracks between the oxide scale and the alloy substrate are noticed, the oxides are prone to separate from the substrate due

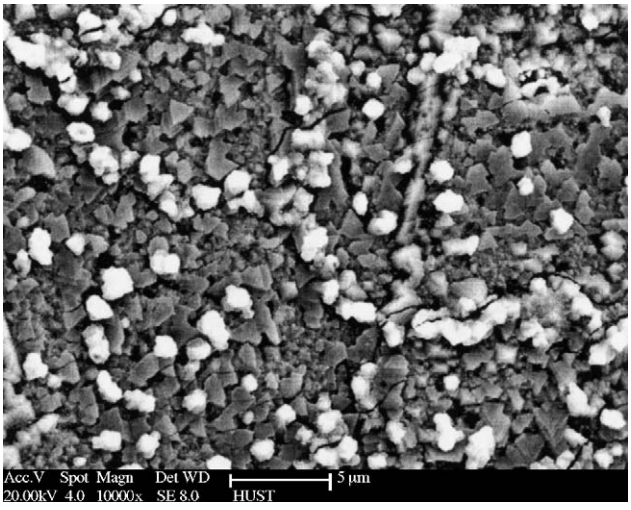

Fig. 7. Higher magnification SEM micrograph of the surface oxide morphology of SS310 after exposure to humidified H_2 at 750 °C for 1000 h, showing well faceted oxide particles inside the grains and rounded particles along the grain boundaries.

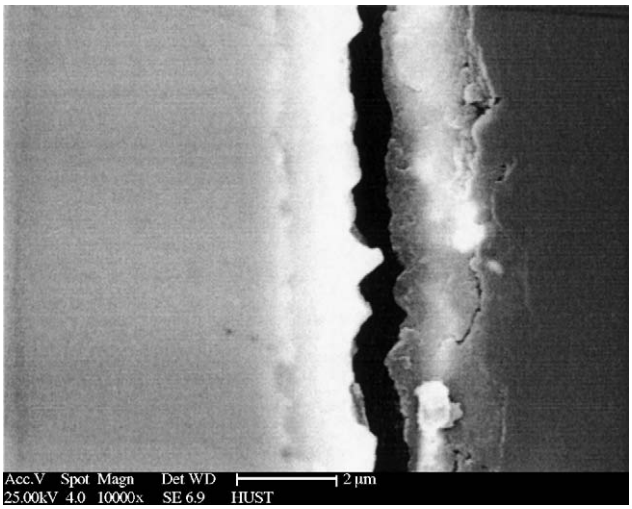

Fig. 8. SEM micrograph of the cross-section of Haynes 230 oxidized in air at 750 °C for 1000 h, showing a oxide scale thickness around 1 μm.

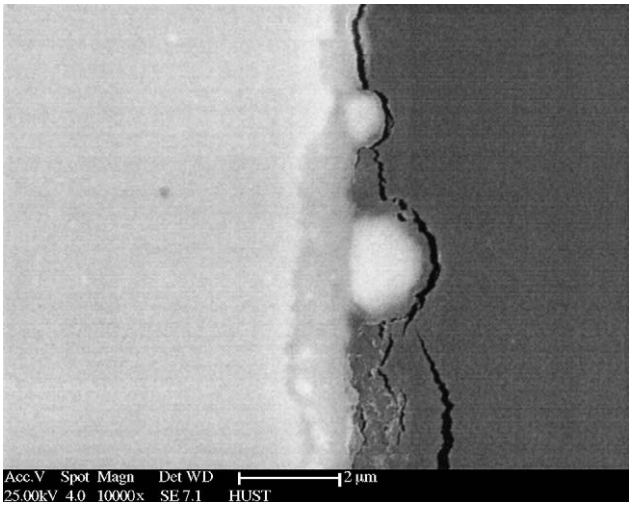

Fig. 9. SEM micrograph of the cross-section of Haynes 230 oxidized in humidified H_2 at 750 °C for 1000 h, showing an oxide scale thickness around 1 μm and metallic nodules.

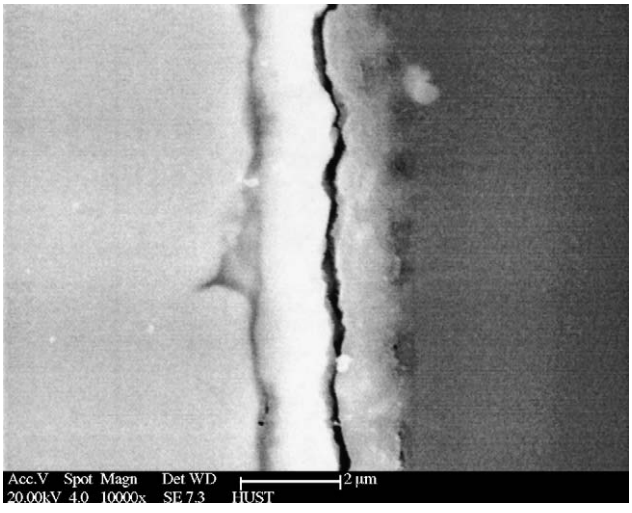

Fig. 10. SEM micrograph of the cross-section of SS310 oxidized in air at 750 °C for 1000 h, showing an oxide scale thickness around 1 μm and cracks between the substrate and the scale.

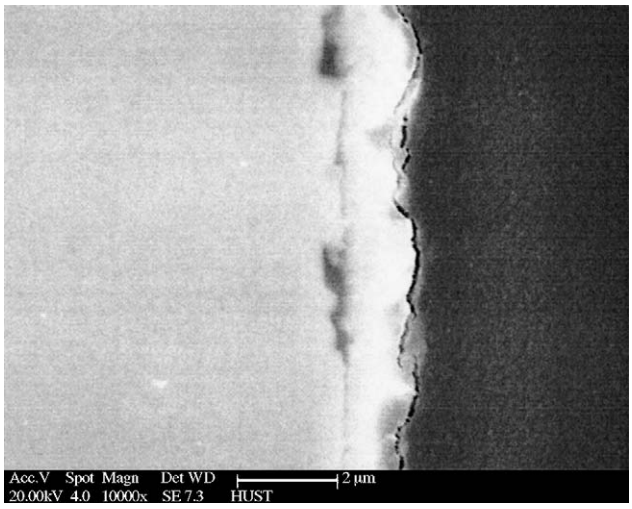

Fig. 11. SEM micrograph of the cross-section of SS310 oxidized in humidified H_2 at 750 °C for 1000 h, showing an oxide scale thickness around 1 μm and cracks between the substrate and the scale.

to a larger mismatch of CTEs between the scale and the base metal.

Figs. 12–15 are the compositional profiles of the oxide scales obtained from oxidized Haynes 230 and SS310 in both air and humidified H_2, respectively, by using EDS line scanning. The line scan started from the alloy substrate and ended right beyond the oxide scale. Within the range of the substrate, the content of each element is consistent with the alloy compositions of Haynes 230 and SS310, such as higher content of Ni in Haynes 230 and Fe in SS310. Inside the well-defined oxide scale as seen in Figs. 8–11, Cr, Mn and O are the dominant elements whose content levels are much higher than that in the base alloys; in contrast, the contents of Ni and Fe reach the minimums, well below the level of that in the substrates, which suggests that the oxide scales contain insignificant amount of Ni and Fe elements. In between the substrate and the well-defined oxide scale, the contents of Cr, Mn and O are gradually increasing while those of Fe and Ni are decreasing, implying that the formation of Cr- and Mn-containing oxide scale expels Fe and Ni from the oxide region. However, the Ni content noticeably increases in Fig. 13 while crossing the nodule and the concentration of other elements is dramatically decreased, which indicates that the nodules are basically Ni (Ni-rich) in the metallic form.

3.3. Phase identification of oxide scales

Both Cr_2O_3 and $MnCr_2O_4$ oxide were identified in all the samples for both alloys oxidized in reducing and oxidizing atmospheres. Figs. 16–19 are the X-ray diffraction patterns obtained from the surfaces of Haynes 230 and SS310 samples oxidized in both air and humidified H_2 environments, respectively, at 750 °C for 1000 h. Since the oxide layer is relatively thin, the intensity of the diffraction peaks generated from Cr_2O_3 and $MnCr_2O_4$ are somewhat weak, and the X-ray penetrated the oxide scale, the information of the substrate was also obtained. Other than the substrate, Cr_2O_3 and $MnCr_2O_4$ phases, NiO may exist in Haynes 230 sample oxidized in air; and metallic Ni (Ni-rich) phase was identified in Haynes 230 sample oxidized in reducing atmosphere, as shown in Fig. 17, corresponding to the metallic nodules seen in Fig. 8 with the composition demonstrated in Fig. 13. For further verification, Fig. 20 is a spot ESD compositional analysis result obtained from a specific well-grown metallic nodule. Ni is the dominant element in the nodule; with trace amount of other elements like Cr, Fe and Mn those either in the nodule or in the surroundings due to the small nodule size. Therefore, it can be concluded that Ni or Ni-rich solid solution was formed during the oxidation of the Ni-based alloy Haynes 230 in simulated SOFC anode environment. In the oxidized SS310 that is a Fe-based stainless steel, no Ni-rich solid solution was identified.

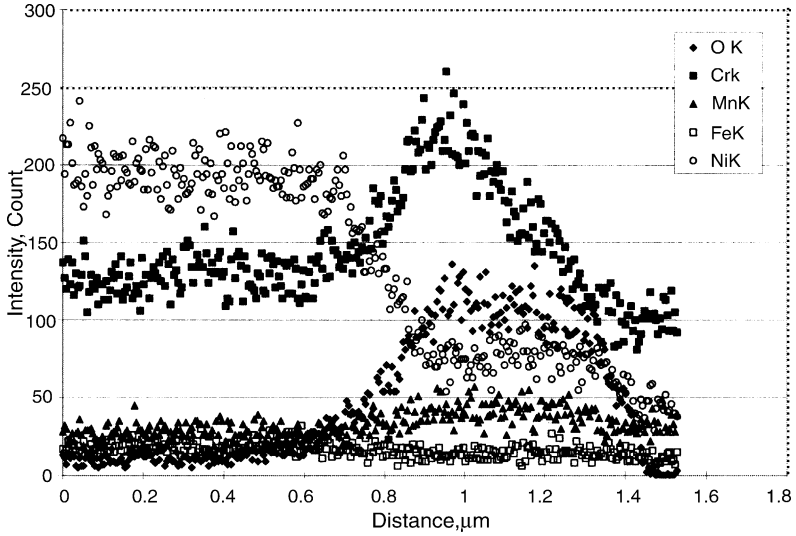

Fig. 12. EDS compositional profile crossing the oxide scale of Haynes 230 exposed to air at 750 °C for 1000 h, showing significant lower Fe and Ni contents in the scale compared to the substrate.

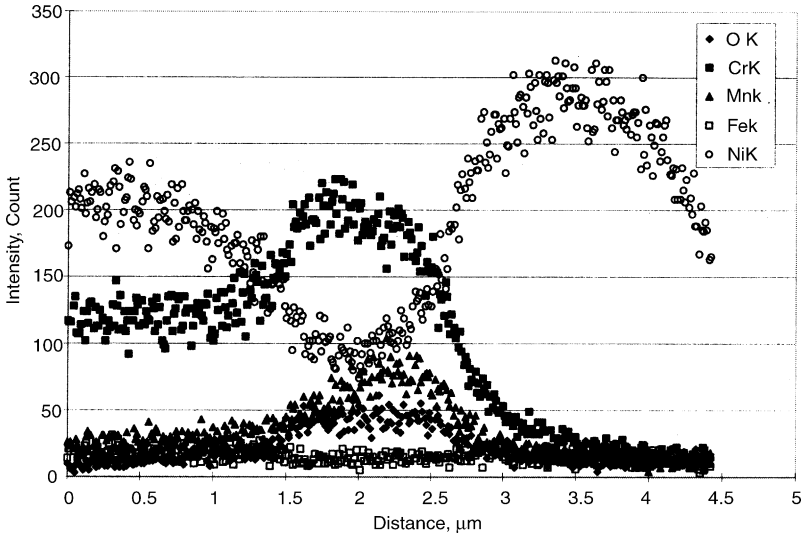

Fig. 13. EDS compositional profile crossing the oxide scale of Haynes 230 exposed to humidified H_2 at 750 °C for 1000 h, showing significant lower Fe and Ni concentrations in the scale compared to the substrate and almost pure Ni in the metallic nodule.

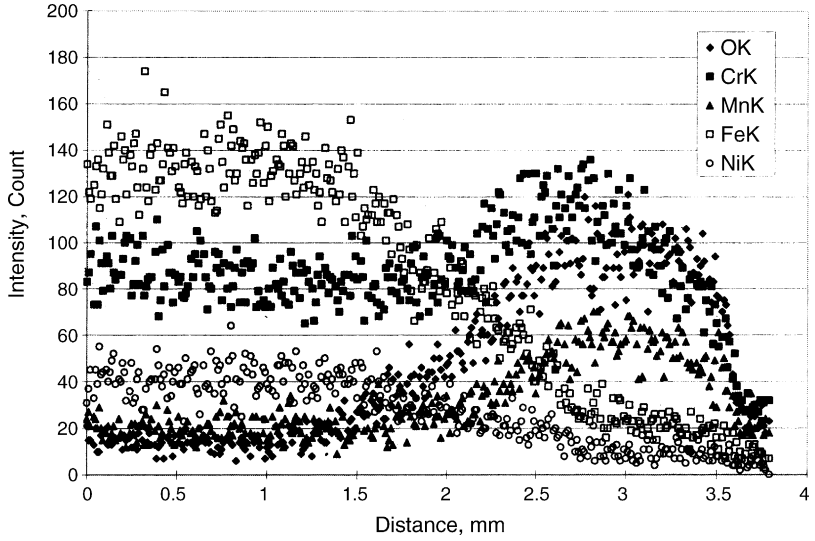

Fig. 14. EDS compositional profile crossing the oxide scale of SS310 exposed to air at 750 °C for 1000 h, showing significant lower Fe and Ni contents in the scale compared to the substrate.

4. Discussion

4.1. Estimation of area specific resistance

Area specific resistance (ASR) associated with the oxide scales of the oxidized alloys can been expressed by

$$\mathrm{ASR} = \rho t \quad (1)$$

where ρ is the electrical resistivity of the oxide, and t is the thickness. Conventionally, an ASR below 0.1 Ω cm^2 contributed by the metallic interconnect materials is acceptable. The reported resistivity values of Cr_2O_3 and $MnCr_2O_4$ at 750 °C are 78 Ω cm [25] and ∼0.5 Ω cm [26], respectively. Assuming Cr_2O_3 is the dominating phase in the oxide scales for all the situations, the ASR estimated will have the highest value, presenting the worst scenario in terms of the application of both alloys studied here as interconnect materials. According to Eq. (1), the ASR after 1000 h of exposure to the simulated SOFC atmospheres at 750 °C is 7.8×10^{-3} Ω cm^2, taking the oxide scale thickness as 1 μm. If the parabolic kinetics applies to the growth of the oxide scale, the scale thickness will be 6.32 μm after 40,000 h of exposure, resulting in an ASR of 4.93×10^{-2} Ω cm^2. Therefore, both Haynes 230 alloy and SS310 stainless steel can be suitable for the interconnect application in a SOFC operated at ∼750 °C. However, SS310 is prone to oxide scale spallation, which will significantly increase the oxidation kinetics with time, further spallation evaluation is desired.

4.2. Formation of Ni (Ni-rich) nodules

Existence of the Ni-rich phase in the oxide scale formed in the simulated SOFC anodic atmosphere was not reported in the previous study [21] where Haynes 230 was oxidized in the

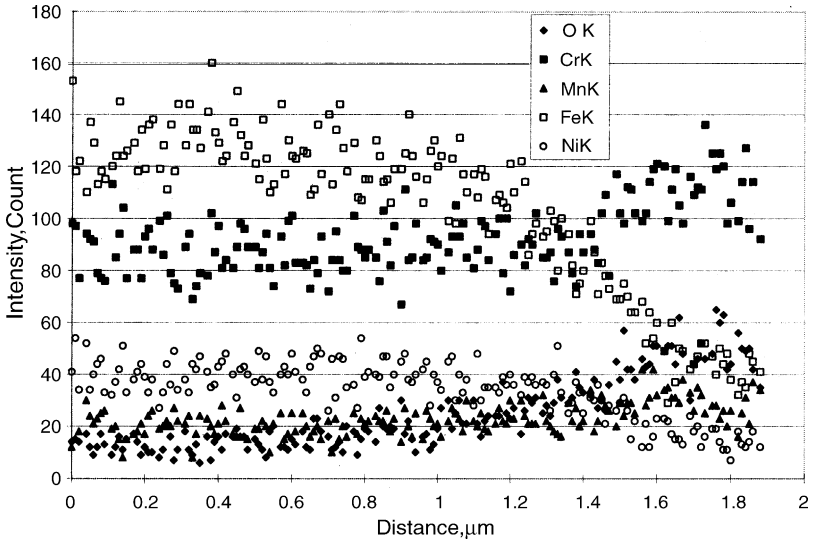

Fig. 15. EDS compositional profile crossing the oxide scale of Haynes 230 exposed to humidified H_2 at 750 °C for 1000 h, showing significant lower Fe and Ni contents in the scale compared to the substrate.

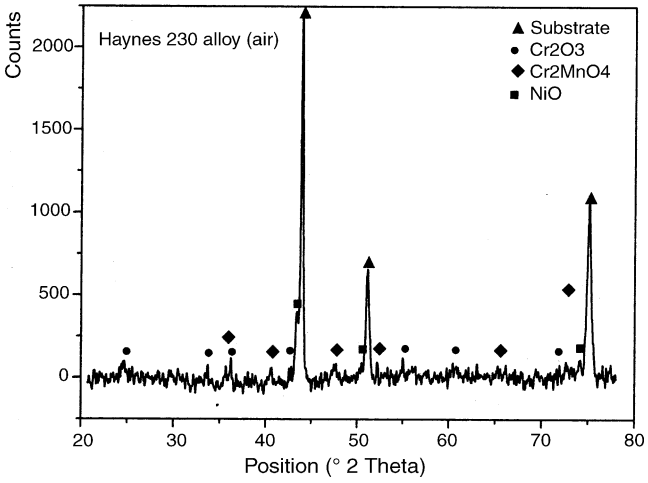

Fig. 16. X-ray diffraction pattern obtained from the surface of Haynes 230 oxidized in air at 750 °C for 1000 h, showing Cr_2O_3, $MnCr_2O_4$, the substrate and possibly NiO phases.

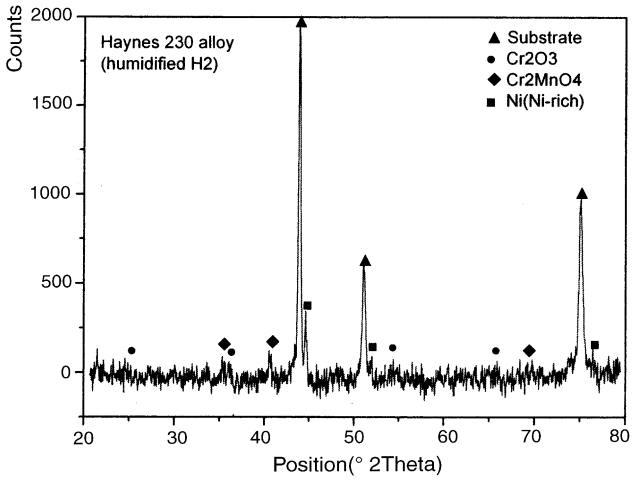

Fig. 17. X-ray diffraction pattern obtained from the surface of Haynes 230 oxidized in humidified H_2 at 750 °C for 1000 h, showing Cr_2O_3, $MnCr_2O_4$, the substrate and pure Ni (Ni-rich) phases.

temperature range of 700–1100 °C for up to 1000 h in humidified H_2. As known, in order to oxidize Ni to form NiO, the oxygen activity must exceed a certain equilibrium value that varies with temperature. At 750 °C, the oxygen partial pressure for forming NiO is $\sim 10^{-16}$ atm [27], which is expected to be much higher than that in the moisturized H_2 used in the present study. For wet hydrogen through a water bubbler, the oxygen partial pressure can be estimated by the following equations [27]:

$$\log p_{H_2O} = -\frac{2961}{T_{bubbler}} - 5.13 \log T_{bubbler} + 21.13 \quad (2)$$

$$p_{O_2} = \left(\frac{p_{H_2O}}{p_{H_2}}\right)^2 \left[\exp\left(\frac{-246000 + 54.8T}{8.314T}\right)\right]^2 \quad (3)$$

In the present study, H_2 was wet through a water bubbler at $T_{bubbler} = 338$ K (65 °C), consequently, the oxygen partial pressure P_{O_2} at $T = 1023$ K (750 °C) was 2.5×10^{-21} atm, much

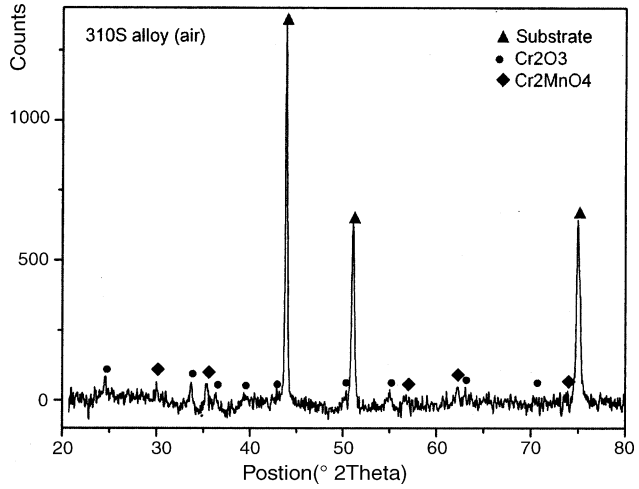

Fig. 18. X-ray diffraction pattern obtained from the surface of SS310 oxidized in air at 750 °C for 1000 h, showing Cr_2O_3 and $MnCr_2O_4$ oxides, and the substrate phase.

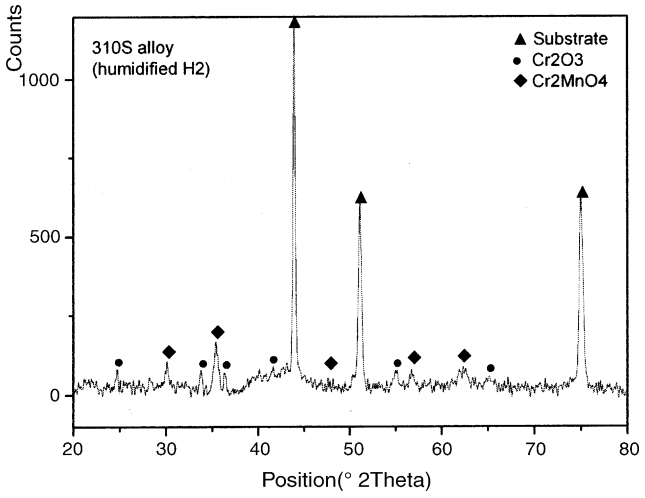

Fig. 19. X-ray diffraction pattern obtained from the surface of SS310 oxidized in humidified H_2 at 750 °C for 1000 h, showing Cr_2O_3 and $MnCr_2O_4$ oxides, the substrate phase.

lower than the required oxygen partial pressure for Ni oxidation at 750 °C, thus Ni remained metallic after 1000 h of exposure to the environment, while Cr and Mn were selectively oxidized. Once Cr_2O_3 is nucleated on the original alloy surface, it grows inwardly by the outward diffusion of Cr ions. The metallic Ni will be expelled and enriched at the alloy/scale interface. Due to the volume expansion associated with the Cr to Cr_2O_3 conversion, the ejected Ni will be under compressive stresses, subsequently diffuse towards the free surface where free energy is low, and form nodules. It is expected that a complete layer of Ni will be formed with further oxidation, as seen in the case of oxidation of superalloys in the molten carbonate fuel cells [28]. At the grain boundaries, the vacancy concentration is significantly higher than that in the grains, and the rejected Ni may remain inside the grain boundaries, instead of forming nodules on top of the surface, less Ni (Ni-rich) nodules are observed. It is noted that the formation of Ni (Ni-rich) nodules only occurs in the Ni-based alloys, such as Haynes 230 in this study, IN-625 and IN-718 in reference [28]. The same phenomenon was not observed in Fe-based alloys, such as SS310 stainless steel.

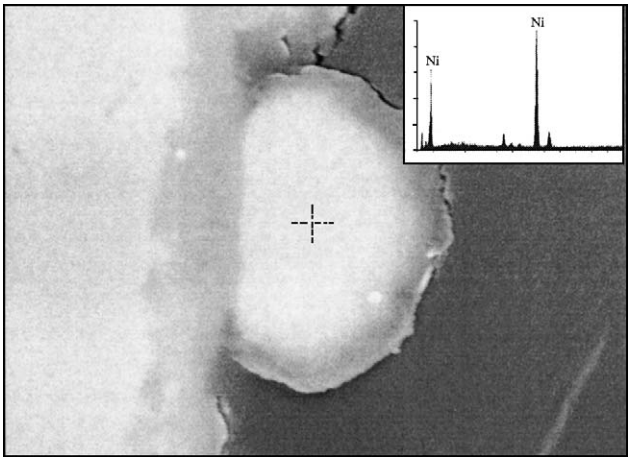

Fig. 20. EDS compositional analysis of the metallic nodule on top of the oxide scale in Haynes 230 oxidized in humidified H_2 at 750 °C for 1000 h, confirming the metallic Ni (Ni-rich) nature of the nodule.

4.3. Cr–Mn spinel formation during oxidation

Formation of Cr–Mn spinels with various compositions, such as $CrMn_2O_4$, $Cr_{1.5}Mn_{1.5}O_4$ and $MnCr_2O_4$, were frequently reported in the oxidation studies of stainless steels and heat resistant alloys for SOFC interconnect applications. Recently, Qu et al. [29] systematically studied this kind of spinels, and found that the electrical conductivity increases with decrease of Cr content. Assuming that Cr_2O_3 forms in the early stage of oxidation and further diffusion of Cr and Mn ions through the Cr_2O_3 layer to form Cr–Mn spinels, the reactions can be simplified as

$$Mn + 2Cr + 2O_2 = MnCr_2O_4 \quad (4)$$

$$2Mn + Cr + 2O_2 = CrMn_2O_4 \quad (5)$$

when forming $MnCr_2O_4$ and $CrMn_2O_4$ spinels. For reactions (4) and (5), the reaction constants are

$$k_{(4)} = \frac{1}{a_{Mn} a_{Cr}^2 p_{O_2}^2} \quad (6)$$

$$k_{(5)} = \frac{1}{a_{Mn}^2 a_{Cr} p_{O_2}^2} \quad (7)$$

where a_{Cr} and a_{Mn} are the activities of Cr and Mn in the Cr_2O_3 layer. The standard Gibbs free energies for the formation of these two spinels are

$$\Delta G^\circ_{(4)} = -RT \ln k_{(4)} \quad (8)$$

$$\Delta G^\circ_{(5)} = -RT \ln k_{(5)} \quad (9)$$

The difference between the standard free energies is

$$\Delta G = \Delta G^\circ_{(4)} - \Delta G^\circ_{(5)} = RT \ln \frac{a_{Cr}}{a_{Mn}} \quad (10)$$

When $a_{Cr} < a_{Mn}$, $\Delta G < 0$ is satisfied, $MnCr_2O_4$ will be the thermodynamically favorable phase, otherwise, $CrMn_2O_4$ forms. Since the diffusion coefficient of Cr in Cr_2O_3 is smaller than that of Mn, i.e, $D_{Cr} < D_{Mn}$ [30], a_{Cr} can be reasonably smaller than a_{Mn}, that is why $MnCr_2O_4$ phase has been frequently reported in relevant studies, even though the Mn concentration in the studied alloys is usually very low.

5. Conclusions

(1) Both Haynes 230 alloy and SS310 stainless steel have acceptable oxidation resistance in both air and humidified H_2 at 750 °C. The oxide scale thickness is around 1 μm after exposure to the environments for 1000 h. Cr_2O_3 and $MnCr_2O_4$ are the dominant phases in the oxide scales, and the estimated ASR is smaller than 0.1 Ω cm^2, the conventionally accepted threshold value.

(2) The calculated oxygen partial pressure in the humidified H_2 atmosphere used in this study is several orders of magnitude

lower than that required for Ni oxidation at 750 °C; the existence of metallic Ni (Ni-rich) phase was confirmed in Haynes 230 alloy after oxidation under such reducing condition. Ni (Ni-rich) nodules were formed on top of the oxide scale due to the selective oxidation of Cr and the associated volume expansion.

(3) $MnCr_2O_4$ is the thermodynamically favorable phase, since the diffusion of Cr ions in Cr_2O_3 is much slower than that of Mn, even though the concentration of Mn in both alloys is very low.

Acknowledgements

This research was financially supported by the National Science Foundation of China under the project contract 50471063, the "863" high-tech project under contract 204AA32G070. The authors would like to thank Mr. Wang Jianjun of Materials Characterization Center of Huazhong University of Science and Technology for SEM assistance and Prof. Zhang Tongjun of Huazhong University of Science and Technology for helpful discussions on thermodynamic analysis.

References

[1] N.Q. Minh, T. Takahashi, Science and Technology of Ceramic Fuel Cells, Elsevier, 1995.
[2] J.M. Ralph, A.C. Schoeler, M. Krumpelt, Materials for lower temperature solid oxide fuel cells, J. Mater. Sci. 36 (2001) 1161–1172.
[3] W.Z. Zhu, S.C. Deevi, Development of interconnect materials for solid oxide fuel cells, Mater. Sci. Eng. A348 (2003) 227–243.
[4] W. Kock, in: Proceedings of the 4th International Symposium on SOFCs (SOFC-IV), the Electrochemical Society, Pennington, NJ, 1995, p 841.
[5] E. Batawi, W. Glatz, W. Kraussler, M. Janousek, B. Doggwiler, R. Diethelm, Oxidation resistance and performance in stack tests of near-net-shaped chromium-based interconnects, in: Proceedings of the Solid Oxide Fuel Cells, the Electrochemical Society, Pennington, NJ, 1999, pp. 731–736.
[6] Y. Larring, T. Norby, Spinel and perovskite functional layers between Plansee metallic interconnect (Cr–5 wt% Fe–1 wt% Y_2O_3) and ceramic $(La_{0.85}Sr_{0.15})_{0.91}MnO_3$ cathode materials for solid oxide fuel cells, J. Electrochem. Soc. 147 (9) (2000) 3251–3256.
[7] W.J. Quadakkers, J. Piron-Abellan, V. Shemet, L. Singheiser, Metallic interconnectors for solid oxide fuel cells—a review, Mater. High Temp. 20 (2) (2003) 115–127.
[8] W.Z. Zhu, S.C. Deevi, Opportunity of metallic interconnects for solid oxide fuel cells: a status on contact resistance, Mater. Res. Bull. 38 (2003) 957–972.
[9] K. Huang, P.Y. Hou, J.B. Goodenough, Characterization of iron-based alloy interconnects for reduced temperature solid oxide fuel cells, Solid State Ionics 129 (2000) 237–250.
[10] K. Huang, P.Y. Hou, J.B. Goodenough, Reduced area specific resistance for iron-based metallic interconnects by surface oxide coatings, Mater. Res. Bull. 36 (2001) 81–95.
[11] T. Brylewski, M. Nanko, T. Maruyama, K. Przybylski, Application of Fe–16Cr ferritic alloy to interconnect for a solid oxide fuel cell, Solid State Ionics 143 (2001) 131–150.
[12] T. Brylewski, K. Przybylski, J. Morgiel, Mater. Chem. Phys. 81 (2003) 434.
[13] T. Brylewski, J. Dabek, K. Przybylski, Oxidation kinetics study of the iron-based steel for solid oxide fuel cell application, J. Thermal Anal. Calorimetry 77 (2004) 207–216.
[14] T. Horita, Y. Xiong, K. Yamaji, N. Sakai, H. Yokokawa, Stability of Fe–Cr alloy interconnectors under CH_4–H_2O atmosphere for SOFCs, J. Power Sources 118 (2003) 35–43.
[15] T. Horita, Y. Xiong, K. Yamaji, N. Sakai, H. Yokokawa, Evaluation of Fe–Cr alloys interconnects for reduced operation temperature SOFCs, J. Electrochem. Soc. 150 (2003) A243–A248.
[16] T. Horita, Y. Xiong, H. Kishimoto, K. Yamaji, N. Sakai, H. Yokokawa, Application of Fe–Cr alloys to solid oxide fuel cells for cost-reduction oxidation behavior of alloys in methane fuel, J. Power Sources 131 (2004) 293–298.
[17] H. Kurokawa, K. Kawamura, T. Maruyama, Oxidation behavior of Fe–16Cr alloy interconnect for SOFC under hydrogen potential gradient, Solid State Ionics 168 (2004) 13–21.
[18] W.A. Meulenberg, S. Uhlenbruck, E. Wessel, H.P. Buchkremer, D. Stöver, Oxidation behavior of ferrous alloys used as interconnecting material in solid oxide fuel cells, J. Mater. Sci. 38 (2003) 507–513.
[19] T. Uehara, A. Toji, K. Inoue, M. Yamaguchi, T. Ohno, Total solution of metallic materials for SOFCs, in: Proceedings of Solid Oxide Fuel Cells VIII, the Electrochemical Society, Pennington, NJ, 2003, pp. 914–922.
[20] D. England, A. Virkar, Oxidation kinetics of some nickel-based superalloy foils and electronic resistance of the oxide scale formed in air, J. Electrochem. Soc. 146 (1999) 3196–3202.
[21] D. England, A. Virkar, Oxidation kinetics of some nickel-based superalloy foils in humidified hydrogen and electronic resistance of the oxide scale formed, J. Electrochem. Soc. 148 (2001) A330–A338.
[22] L. Jian, P. Jian, X. Jianzhong, Q. Xiaoliang, Oxidation of Haynes 230 alloy in reduced temperature solid oxide fuel cell environments, J. Power Sources 139 (2005) 182–187.
[23] Haynes 230 Alloy Product Brochure, Haynes International.
[24] Fuel Cell Handbook, The US Department of Energy, 2004.
[25] G.V. Samsonov, The Oxide Handbook, translated from Russian by C. Nigel Turton, T. Turton, IFI/Plenum, 1973.
[26] A.V. Virkar, U.S. Patent 6,054,231, April 25, 2000.
[27] D. Gaskell, Introduction to Metallurgical Thermodynamics, second ed., McGraw-Hill Book Company, 1981.
[28] L. Jian, C.Y. Yuh, M. Farooque, Oxidation behavior of superalloys in oxidizing and reducing environments, Corrosion Sci. 42 (2000) 1573–1585.
[29] W. Qu, L. Jian, J.M. Hill, D.G. Ivey, Electrical and microstructural characterization of spinel phases as potential coatings for SOFC metallic interconnects, J. Power Sources 153 (2006) 114–124.
[30] R.E. Lobnig, H.P. Schmidt, K. Hennesen, H.J. Grabke, Diffusion of cations in chromia layers grown on iron-based alloys, Oxidation Met. 37 (1/2) (1992) 81–93.